doi: 10.1038/nature06232

SUPPLEMENTARY INFORMATION

Open to closed transition in *apo* maltose-binding protein visualized by paramagnetic NMR

Chun Tang,[1] Charles D. Schwieters[2] and G. Marius Clore[1]

[1]Laboratory of Chemical Physics, Building 5, National Institute of Diabetes and Digestive and Kidney Diseases, National Institutes of Health, Bethesda, Maryland 20892-0520, U.S.A.
[2]Division of Computational Bioscience, Building 12A, Center for Information Technology, National Institutes of Health, Bethesda, Maryland 20892-5624, U.S.A.

1. Impact of the existence of a minor population of *holo* (maltotriose-bound) conformation on the agreement between observed and calculated RDCs for *apo* MBP, assuming only a single conformation represented by the crystal structure of *apo* MBP.

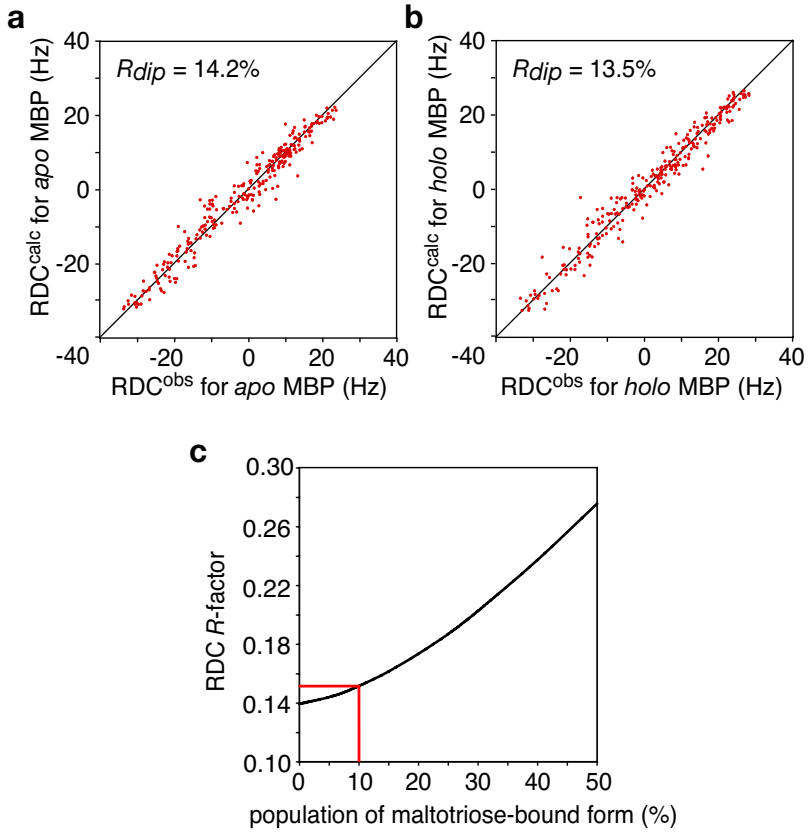

Fig. S1. Agreement between observed and calculated RDCs for MBP. a, Correlation between observed $^{1}D_{NH}$ RDCs measured for *apo* MBP with calculated values obtained by SVD using the coordinates of the crystal structure of *apo* MBP (1OMP). The magnitude of the principal component of the alignment tensor (D_a^{NH}) and the rhombicity (η) are 16.2 Hz and 0.25, respectively. **b,** Correlation between observed $^{1}D_{NH}$ RDCs measured for *holo* MBP with calculated values obtained by SVD using the coordinates of the crystal structure of *holo* MBP (3MBP). The values of D_a^{NH} and η are 16.4 Hz and 0.41, respectively. **c,** RDC *R*-factor (R_{dip}) obtained by SVD against a set of RDCs generated by a population weighted average of the experimental RDCs for *apo* and *holo* MBP assuming a single conformation represented by the crystal structure of apo MBP (1OMP). With a contribution of 10% from RDCs for *holo* MBP, the RDC *R*-factor is only increased from 14% to 15%. The experimental RDCs for *holo* and *apo* MBP were taken from ref. 10 (main text) and were kindly provided by Dr. Lewis Kay.

2. Small angle X-ray scattering for *apo* MBP.

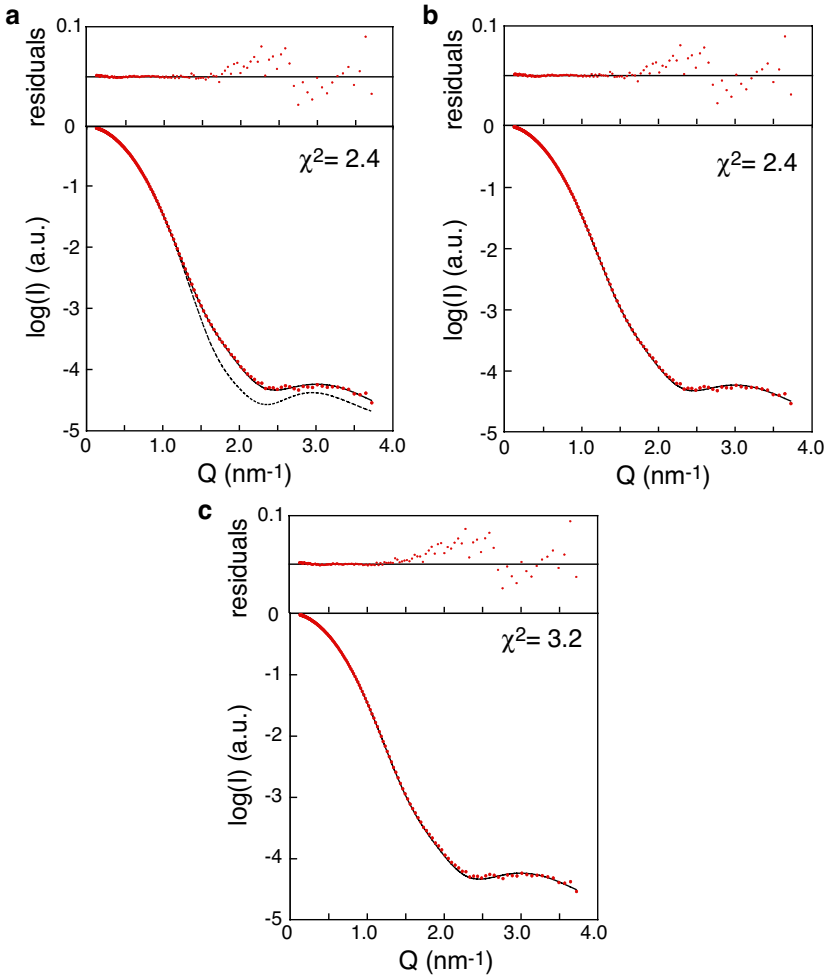

Fig. S2. Comparison between observed and theoretical SAXS curves for *apo* MBP. The experimental data are shown as red circles and the theoretical curves (solid lines) calculated from the coordinates of **a,** the crystal structure of *apo* MBP (1OMP); **b,** a mixture of 95% open form *apo* MBP (1OMP) and 5% minor species derived from the PRE data; and **c,** a mixture of 95% open form *apo* MBP (1OMP) and 5% *holo* (maltotriose-bound) MBP (3MBP). Also shown in (**a**) as a dashed line is the theoretical curve computed from the crystal structure of *holo* MBP (3MBP). The theoretical scattering intensity in (b) and (c) is given by $I^{calc}_{mixture} = 0.95 \times I^{calc}_{apo} + 0.05 \times I^{calc}_{minor}$, where I^{calc}_{minor} is the theoretical scattering intensity of the minor species, either the minor form derived from the PRE data or *holo* MBP, and I^{calc}_{minor} for the minor form at each scattering angle is the average over the 50 final structures. The χ^2 between observed and theoretical curves remains the same upon incorporation of a 5% contribution of the minor form structure derived from the PRE data, but is increased to 3.2 upon inclusion of a 5% contribution of the *holo* MBP crystal structure. The latter can be attributed to a systematic deviation between observed and calculated scattering intensities between Q = 1.32-1.68 nm^{-1}.

3. Comparison of structure and ligand-binding properties of wildtype *apo* MBP and maleimide-TEMPO conjugated *apo* MBP (D41C).

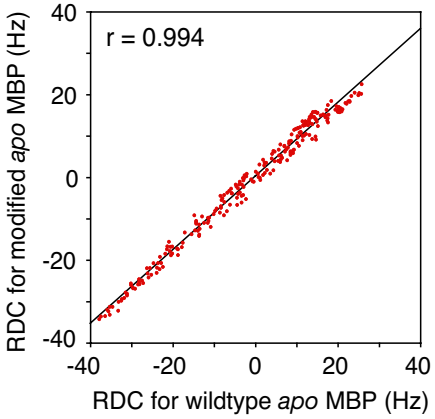

Fig. S3 Correlation between $^{1}D_{NH}$ RDCs measured for the wildtype and D41C spin-labeled *apo* MBP. The alignment medium comprises ~15 mg/ml phage pf1. The excellent correlation between the two sets of RDCs (correlation coefficient r = 0.994) indicates that the backbone coordinates for the wildtype and modifed *apo* MBP are identical within measurement error. [Note that the small deviation in the slope (k = 0.89) from a value of 1.0 is due to slightly different concentrations of pf1 in the two samples].

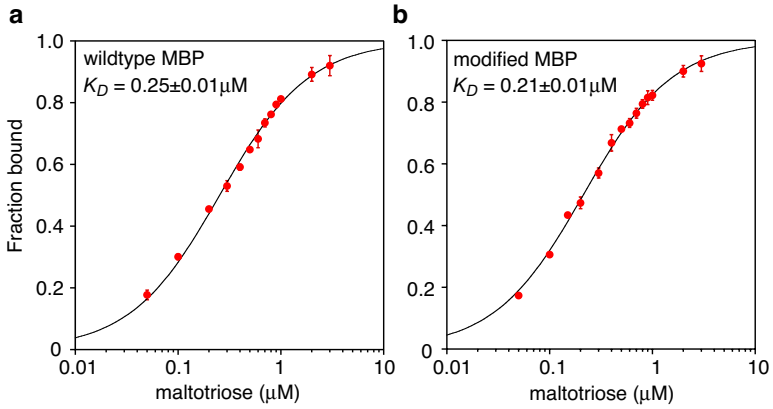

Fig. S4. Binding affinity of maltotriose for MBP monitored by fluorescence. a Wildtype MBP; **b,** D41C MBP mutant conjugated to maleimide-TEMPO. Fluorescence measurements were carried out using a Jobin Yvon Fluoromax-3 fluorimeter with an excitation wavelength of 280 nm and an emission wavelength of 349 nm. The experimental data (shown as red circles) are the averages of two separate measurements and the best-fit curves using a simple binding isotherm are shown as solid lines. The equilibrium dissociation constants for wildtype (~0.25 μM) and nitroxide spin-labeled (~0.21 μM) MBP are the same within experimental error, and in agreement with the previously reported value of ~0.2-0.3 μM for wild type MBP (ref. 8, main text). Error bars: ±1S.D.

4. Comparison between the observed and calculated PREs for *apo* and *holo* MBP.

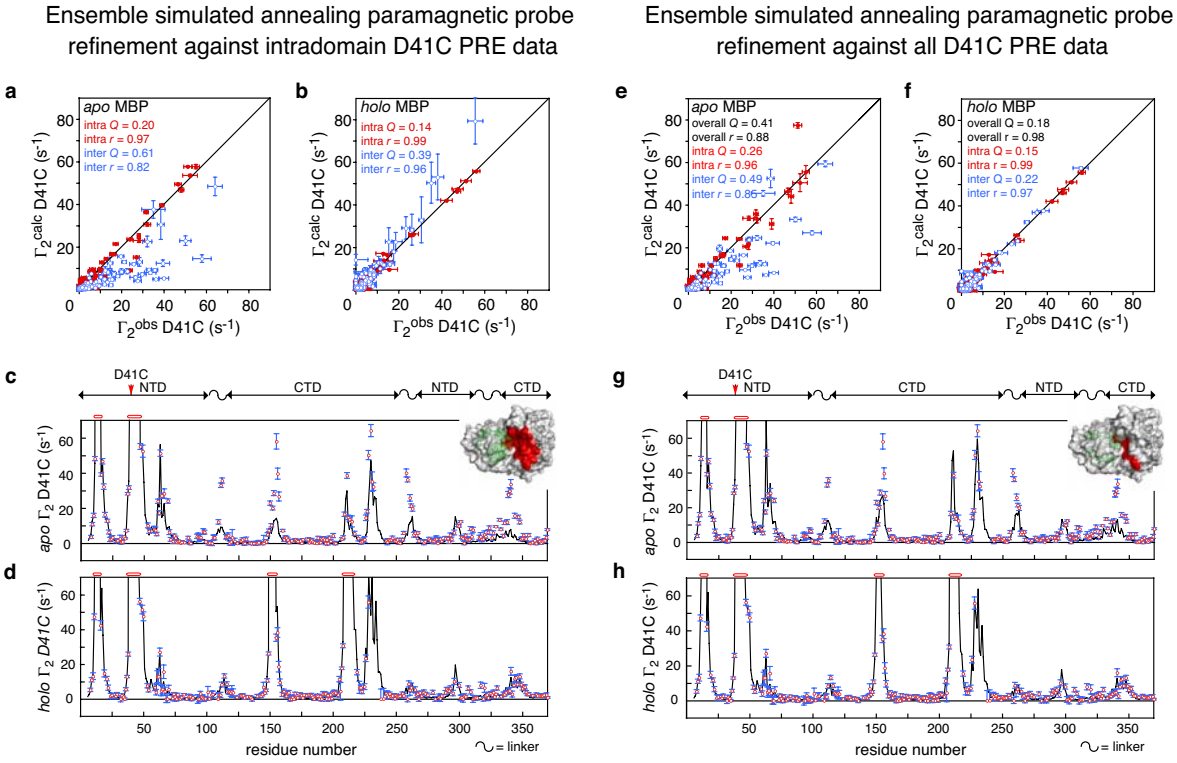

Fig. S5 PRE data obtained for *apo* and *holo* MBP with maleimide-TEMPO spin-label conjugated at D41C. Correlations between observed and calculated PREs for *apo* (**a, e**) and *holo* (**b, f**) MBP, respectively. The PREs are calculated by simulated annealing refinement of the conformational space occupied by the paramagnetic probe against either the intradomain PRE data (**a-d**) or all the PRE data (**e-g**) and are averaged over 100 independent calculations. The intra- (NTD) and inter-domain (CTD plus linker) PREs are shown as red and blue circles, respectively. Comparison of observed (red circles) with the calculated PRE profiles (black lines) for *apo* (**c, g**) and *holo* (**d, h**) MBP, respectively**.** Residues with $^{1}H_N/^{15}N$ cross-peaks completely broadened out are denoted by open red bars. The red arrow indicates the D41C conjugation site of the spin-label. The insets in **c** and **g** display a molecular surface of *apo* MBP, with the conformational space sampled by the oxygen atom of the nitroxide group bearing the unpaired electron displayed as a green mesh, and the residues exhibiting large PRE discrepancies ($\Gamma_2^{obs} - \Gamma_2^{calc} > 10s^{-1}$) colored in red (residues 111-112, 150-157, 209-211, 226-232, 258-262 and 339-348 in **c**, and residues 111-112, 155-157, 258-259 and 339-341 in **g**). Error bars, ±1 S.D.

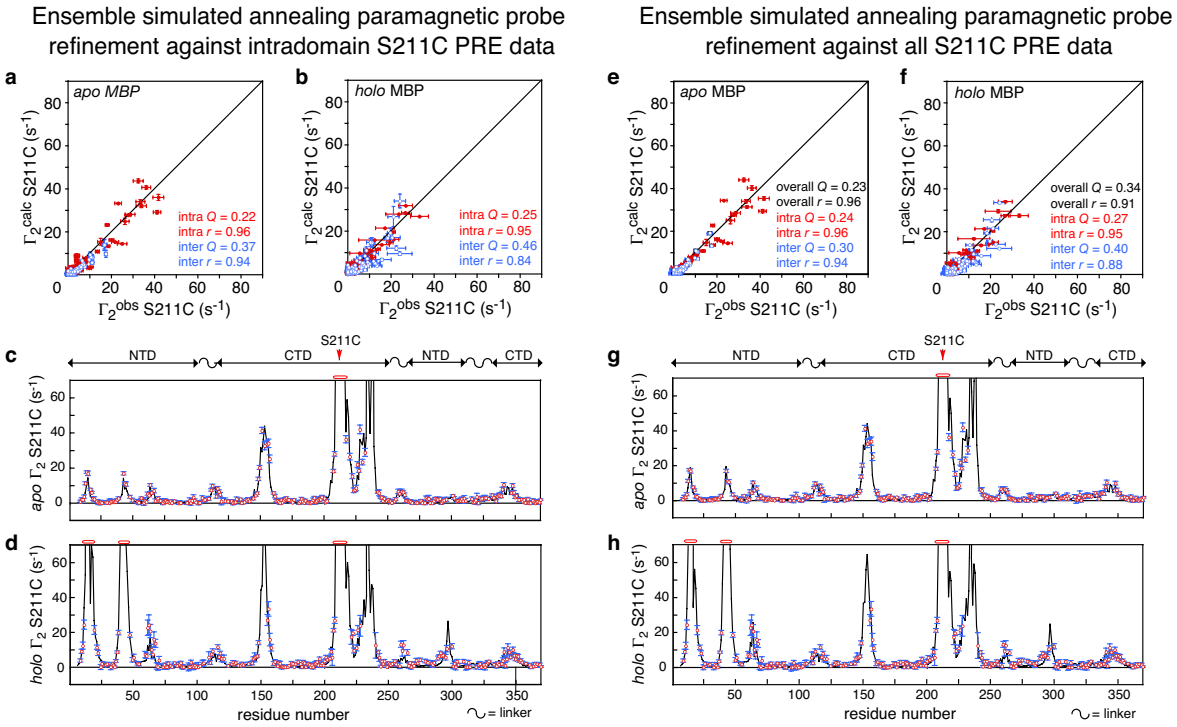

Fig. S6 PRE data obtained for *apo* and *holo* MBP with maleimide-TEMPO spin-label conjugated at S211C. Correlations between observed and calculated PREs for *apo* (**a, e**) and *holo* (**b, f**) MBP, respectively. The PREs are calculated by simulated annealing refinement of the conformational space occupied by the paramagnetic probe against either the intradomain PRE data (**a-d**) or all the PRE data (**e-g**) and are averaged over 100 independent calculations. The intra- (CTD) and inter-domain (NTD plus linker) PREs are shown as red and blue circles, respectively. Comparison of observed (red circles) with the calculated PRE profiles (black lines) for *apo* (**c, g**) and *holo* (**d, h**) MBP, respectively**.** Residues with $^{1}H_N/^{15}N$ cross-peaks completely broadened out are denoted by open red bars. The red arrow indicates the S211C conjugation site of the spin-label. Error bars, ±1 S.D.

5. Comparison of intradomain PREs observed for *apo* and *holo* spin-labeled MBP.

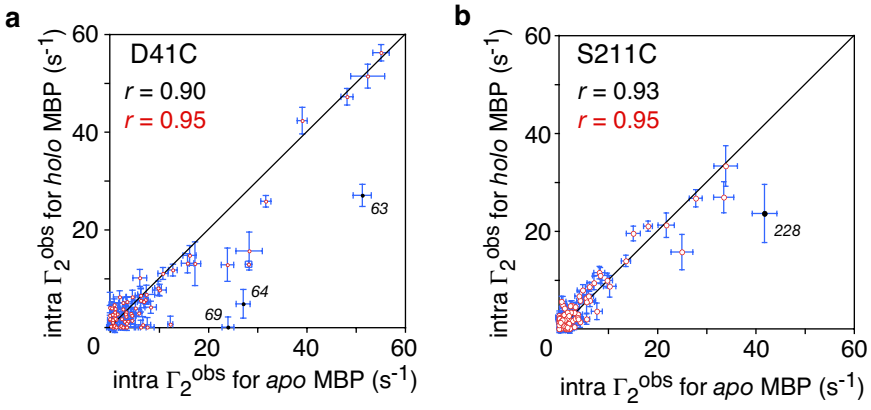

Fig. S7. Correlation between intradomain ^1H_N-Γ_2 rates observed for *apo* and *holo* MBP with maleimide-TEMPO conjugated at (a) D41C and (b) S211C. The overall correlation coefficient is 0.90 and 0.93, for D41C and S211C conjugation sites, respectively. Excluding residues 63, 64 and 69 for the D41C data and residue 228 for the S211C data (colored in black) that are located in close proximity to the other domain in the *holo* state, the correlation coefficients are both improved to 0.95. The excellent agreement between the measured intradomain PREs for *apo* and *holo* MBP indicates that, as expected, the structures of the NTDs and CTDs in the *apo* and *holo* states are unchanged, and the conformational space sampled by the spin-label is similar. Small, subtle differences in the conformational space sampled by the spin-label, however, do occur as a result of domain closure in the *holo* state that account for the PRE discrepancies involving residues 63, 64, 69 and 228. Error bars, ±1 S.D.

6. Conformational space sampled by the maleimide-TEMPO spin-label.

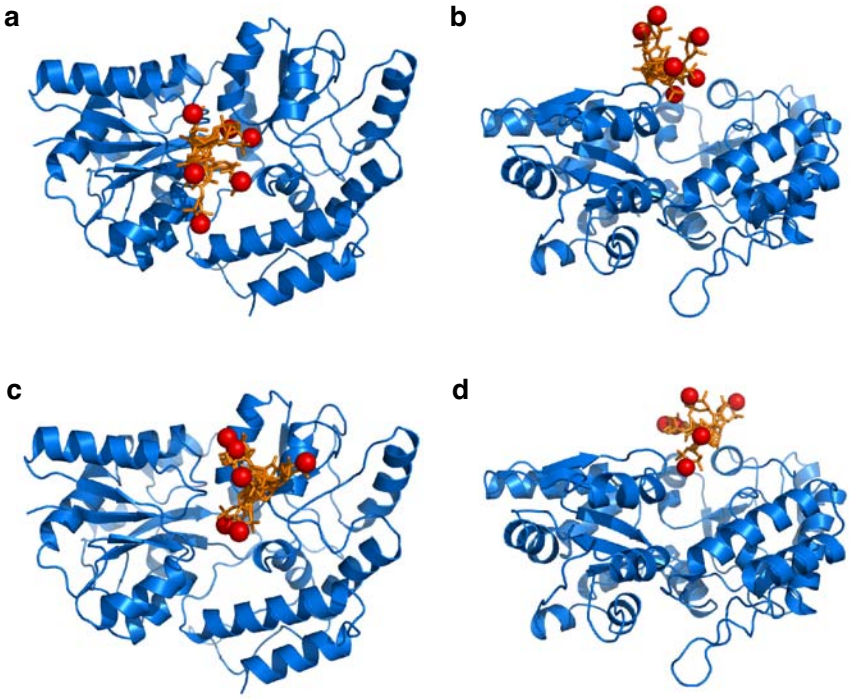

Fig. S8. Two orthogonal views illustrating the conformational space sampled by a six-conformer representation of the maleimide-TEMPO spin-label conjugated to *holo* MBP at (a and b) D41C and (c and d) S211C obtained by simulated annealing refinement against all observed PRE data. The paramagnetic probe is represented by a total of six conformers, three for each enantiomer: the Cys side chain and maleimide-TEMPO are shown as orange sticks, and the oxygen atom of the nitroxide group bearing the unpaired electron is displayed as a red sphere. The coordinates of the crystal structure of *holo* MBP (3MBP) are held fixed and the protein backbone is displayed as a blue ribbon.

7. Exclusion of a solvent PRE effect and other potential intermolecular effects.

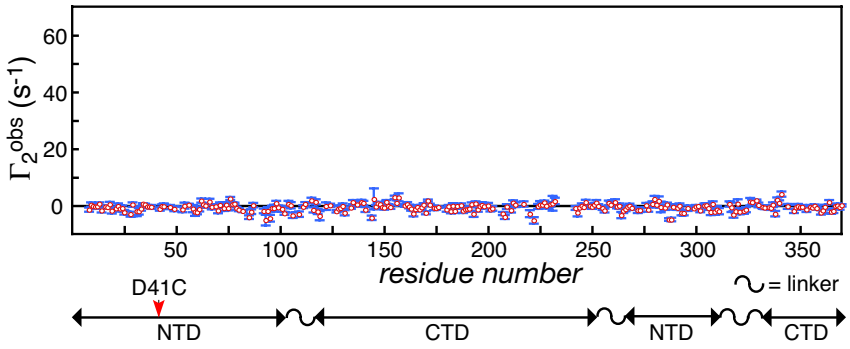

Fig. S9 No intermolecular PREs are observed for a 1:1 mixture of nitroxide spin-labeled *apo* MBP (D41C) at natural isotopic abundance and U-[^{15}N/^{2}H]-labeled wildtype MBP (0.5 mM each). Since the pulse sequence used to measure the $^{1}H_N$-R_2 rates is based on 2D ^{1}H-^{15}N correlation spectroscopy, the PRE in this experiment can only arise from an intermolecular effect involving either random collisions or non-specific interactions between spin-labeled *apo* MBP at natural isotopic abundance and U-[^{15}N/^{2}H]-labeled *apo* MBP. The absence of any observable PREs excludes the presence of any significant intermolecular effects. The red arrow denotes the conjugation site of the spin-label. Error bars, ± 1 S.D.

8. Conjoined rigid body/torsion angle simulated annealing refinement against the PRE data for nitroxide spin-labeled *apo* MBP using a single structure representation.

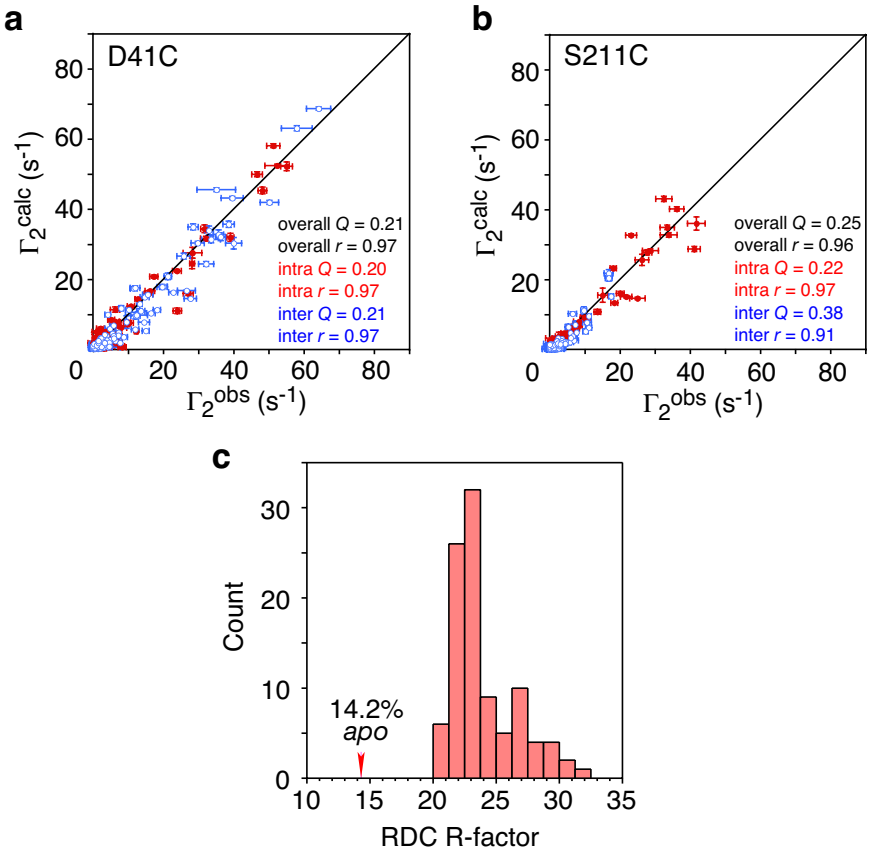

Fig. S10. Agreement between observed and calculated PRE and RDC obtained upon conjoined rigid body/torsion angle simulated annealing refinement against all the experimental PRE data for D41C and S211C nitroxide spin-labeled *apo* MBP using a single structure representation. The excellent correlation between observed and calculated PRE values for the (**a**) D41C and (**b**) S211C data indicates that a single structure representation differing from the crystal structure of *apo* MBP in the relative orientation of the two domains can account for the experimental PRE data. Error bars, ±1 S.D. **c,** The histogram of RDC *R*-factors ($^1D_{NH}$ RDCs not included in the refinement), however, for the ensemble of 100 calculated structures indicates unambiguously that the single structure representation (RDC *R*-factor = 24.0±2.6%) is inconsistent with the experimental RDC data. For reference the dipolar coupling *R*-factor for the *apo* crystal structure (1OMBP), indicated by the red arrow, is 14.2% (cf. Fig. S1a).

9. The minor form structure of *apo* MBP calculated from the PRE data measured on spin-labeled D41C and S211C mutants by conjoined rigid body/torsion angle simulated annealing.

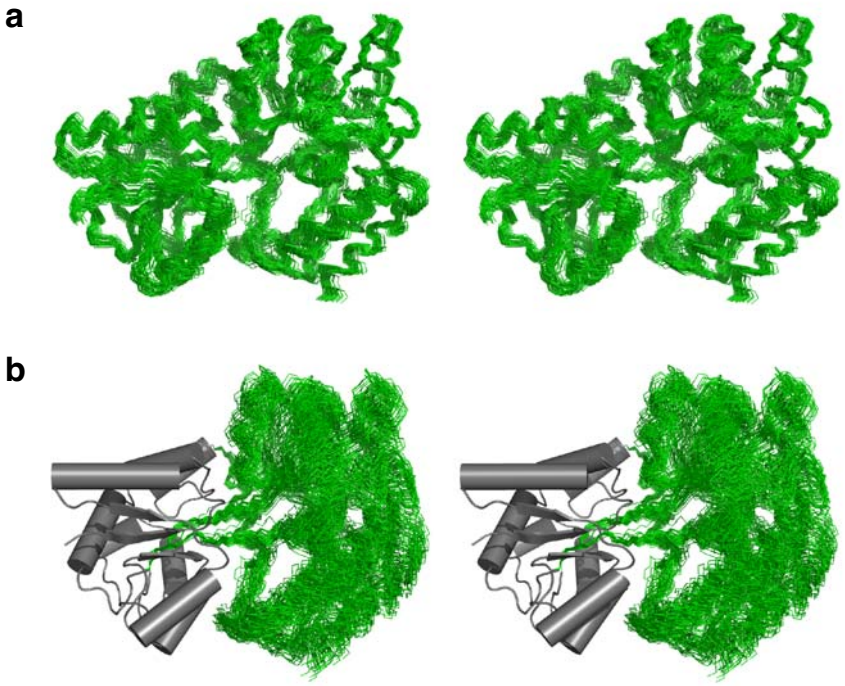

Fig. S11. The minor partially-closed form structure of *apo* MBP. a, Stereoview showing a superposition of the backbone (N, Cα, C) atoms of the 50 final structures best-fitted to both the NTD and CTD. **b,** Stereoview showing a superposition of the CTD backbone (green) of the 50 final structures best-fitted to the NTD (shown as grey cylinders).

10. Three-conformer ensemble representation of the minor form *apo* MBP.

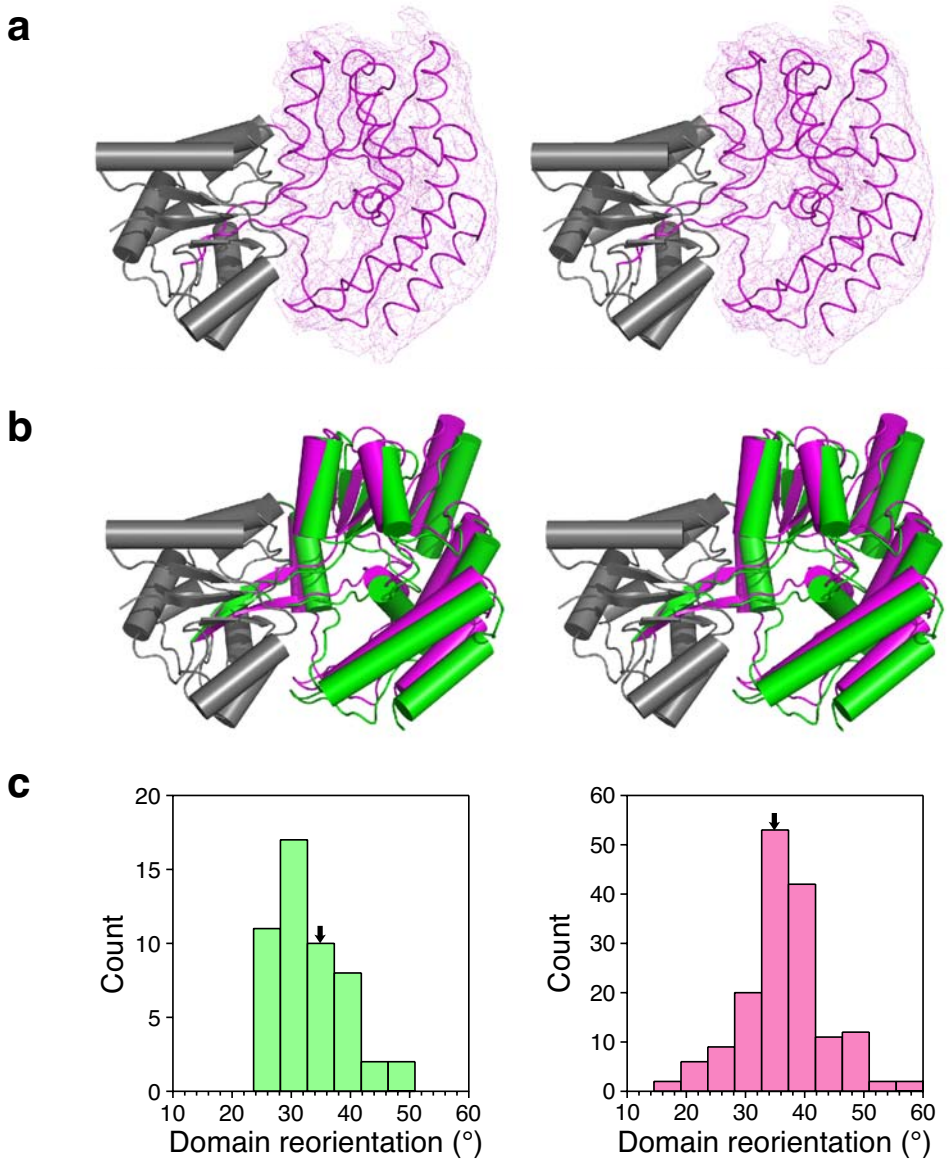

Fig. S12. Three-conformer representation of the minor species yields essentially the same average structure and distribution as the one-conformer representation. a, Stereoview of minor species structure of *apo* MBP calculated using a three-conformer representation. The NTD is superimposed and shown as grey cylinders, the CTD and linker of the average structure are shown as a magenta worm, and the reweighted atomic probability map for the backbone heavy atoms of the CTD and linker residues, plotted at 20% threshold, is shown as magenta meshes. **b**, Stereoview showing a comparison in the relative orientation of the CTD for the average coordinates of the minor form structure calculated with either a single (green cylinders) or three-conformer (magenta cylinders) representation, with the NTD best-fitted (shown as grey cylinders). The orientation of the CTD (relative to a fixed NTD) for the average coordinates of the minor *apo*

form derived from the single and three-conformer representations differs by 8.5°. For comparison, the precision with which the orientation of the CTD relative to the NTD is determined is 16.0±7.3° for the three-conformer representation versus 10.5±4.0° for the single conformer representation. Thus, although the conformational space sampled by the three-conformer representation is somewhat larger than the single one, the structures calculated for the two representations overlap and the mean coordinate positions are similar. Note that the lower precision with which the relative domain orientation is determined in the three- versus single-conformer representation for the minor species is due to the fact that not all members of the three-conformer ensemble need to contribute to the observed interdomain PREs. Thus, for example, a situation in which one of the three members of the ensemble does not contribute to the interdomain PREs, owing to a more open conformation, is equivalent, in the context of the single conformer representation, to a reduction in the population of minor species. Q_{PRE} for the three-conformer representation is 0.22±0.01 and 0.24±0.02 for the D41C and S211C PRE data, respectively; the corresponding values for the single conformer representation are 0.22±0.01 and 0.24±0.01, respectively. **c,** Histogram of the distribution of domain reorientation angles between the open form of *apo* MBP (1OMP) and the minor form for the single conformer (left-hand panel, green; 33.3±6.7°) and three-conformer (right-hand panel, magenta; 36.5±7.2°) representations (positions of mean indicated by arrows). (The domain reorientation angle is obtained by superimposing the NTD domains first and then calculating the rotation required to superimpose the CTD domains).

11. Cross-validation: comparison of minor species calculated by refinement against D41C PRE data alone versus both the D41C and S211C PRE data.

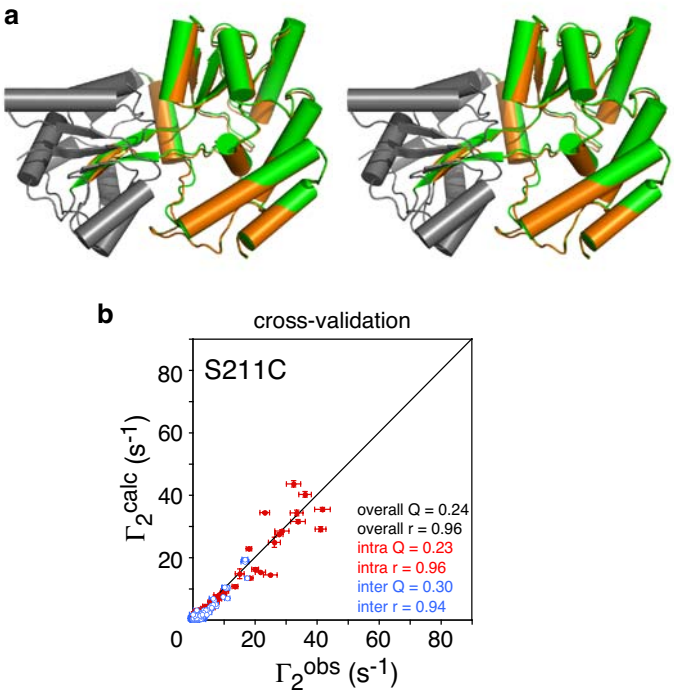

Fig. S13. Cross-validation and comparison of mean coordinates of the minor species of *apo* MBP obtained by conjoined rigid body/torsion angle simulated annealing refinement against the D41C PRE data alone versus the D41C and S211C PRE data. Since the PRE data for S211C are consistent with the open *apo* state they cannot be used to calculate a structure of the minor state on their own. However, the S221C PRE data can be used for cross-validation by calculating a set of structures using only the D41C PRE data. **a**, Stereoview showing the very close similarity in relative orientation of the CTD of the minor *apo* MBP structure (average coordinates) calculated from the D41C PRE restraints alone (orange cylinders) versus that obtained by joint refinement against both D41C and S211C PRE data (green cylinders), with the coordinates of the NTD best-fitted (grey cylinders). The orientation of the CTD (relative to a fixed NTD) differs by only 3° in the two average structures, while the precision with which the orientation is determined is 12.1±4.9° for the structure refined against the D41C data alone versus 10.5±4.0° for the structure refined against both the D41C and S211C data. **b**, Correlation between observed and cross-validated PREs for S211C spin-labeled *apo* MBP. The PREs are calculated by optimizing the conformational space sampled by the paramagnetic probe against all the PRE data while fixing the protein coordinates of the major (1OMP, 95%) and minor (calculated from the D41C PRE data alone, 5%) forms of *apo* MBP. The intra- (CTD) and inter-domain (NTD plus linker) PREs are shown as red and blue circles, respectively. The cross-validated S211C PRE Q-factors and correlations coefficients are essentially the same as those obtained by joint refinement against both the D41C and S211C PRE data (cf. Fig.3c). For comparison, introduction of 5% *holo* MBP results in an increase in the interdomain S211C Q_{PRE} from 0.30 to 0.45 (cf. Fig. 2d). The D41C Q_{PRE} for the structures refined against only the D41C data is 0.22±0.01. Error bars, ±1 S.D.

12. Qualitative cross-validation by evaluation of PREs observed for *apo* MBP using the EDTA-Mn^{2+} paramagnetic probe conjugated to D41C.

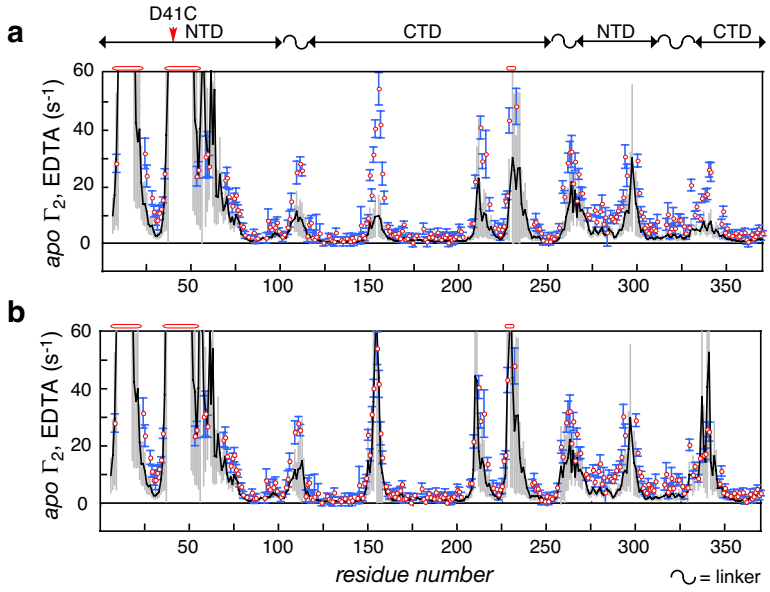

Fig. S14. Qualitative cross-validation of the observed PREs arising from EDTA-Mn^{2+} conjugated to D41C MBP using forward-calculation of PREs. A quantitative analysis by direct refinement against the EDTA-Mn^{2+} D41C PRE data is precluded because many more cross-peaks within the NTD (intradomain) in the vicinity of the paramagnetic probe are broadened beyond the limits of detection owing to the ~4 times larger PRE effect of Mn^{2+} relative to nitroxide. As a result there are insufficient PRE data available within the NTD to sufficiently restrain the optimized distribution of the EDTA-Mn^{2+} ensemble to something reasonable, rather than a highly biased, skewed distribution oriented towards the CTD. However, a forward-calculation strategy can readily be employed for qualitative cross-validation. This entails forward-calculation of Γ_2 rates by randomizing the coordinates of the EDTA-Mn^{2+} paramagnetic probe within the confines imposed by stereochemistry and covalent geometry (without any optimization). The EDTA-Mn^{2+} paramagnetic label, conjugated via a disulfide linkage as described previously (ref. 15, main text), was represented by a three-conformer ensemble. The forward-calculated PREs are averaged from 100 independent calculations. **a,** Comparison of the observed PRE profile (red circles, blue error bars, ±1 S.D.) for *apo* MBP arising from EDTA-Mn^{2+} with the forward-calculated average values (black lines; grey error bars, ±1 S.D.) obtained from the crystal structure of *apo* MBP (1OMP). While the intra-domain PREs within the NTD are well predicted, there is poor agreement for the interdomain PREs within the CTD and linker regions with residues 109-112, 150-158, 209-215, 226-232, 258-265 and 336-341 exhibiting experimental PREs that are significantly larger than the forward-calculated ones ($\Gamma_2^{obs} - \Gamma_2^{calc} > 10 s^{-1}$). **b,** The discrepancies observed in (**a**) are largely resolved by introducing a 5% population of the minor species calculated by conjoined rigid body/torsion angle simulated annealing refinement against the PRE data obtained for D41C and S211C nitroxide spin-labeled *apo* MBP. The forward calculated values in (**b**) represent the average derived from the ensemble of 50 simulated annealing structures calculated for the minor species (i.e. 100 sets of randomized paramagnetic label coordinates for each minor species structure = 5000 sets of coordinates).

13. The value of D_a^{NH} for the major and minor forms of *apo* MBP derived by SVD using RDC data are inversely proportional to their respective populations.

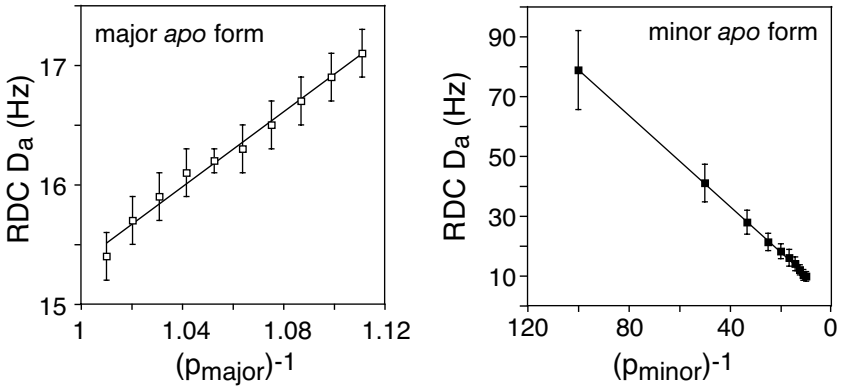

Fig. S15. Correlation between the magnitude of the axial component of the alignment tensor, D_a^{NH}, and the reciprocal of population derived from SVD analysis against the RDC data for *apo* MBP. (p_{major} and p_{minor} are the populations of the major and minor species, respectively, and p_{major} = 1-p_{minor}). Note that fitting the RDC data to a linear combination of major (open) and minor (partially-closed from PRE data) species results in a small decrease in the RDC *R*-factor from 14.2 to 14.0±0.06%. Error bars, ±1 S.D.

14. Interdomain electrostatic interactions in the different conformations of MBP.

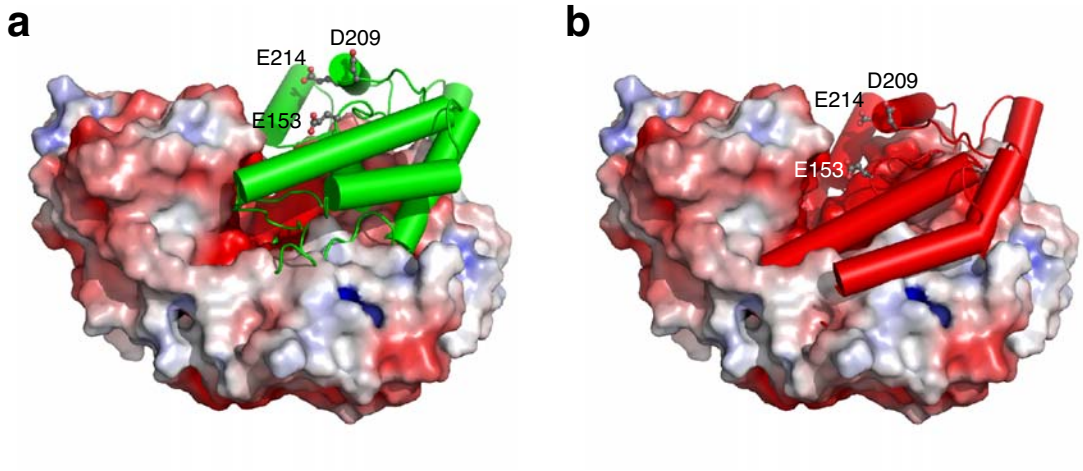

Fig. S16. Interdomain electrostatic interactions. In both (**a**) and (**b**) *apo* MBP is displayed as a molecular surface color-coded according to electrostatic potential (plotted at ±5*kT* with negative potential colored in red, and positive in blue). The sugar binding surface comprising residues in both the NTD and CTD is highly negatively charged. The location of the CTD in the minor partially-closed form of *apo* MBP (green cylinders) and *holo* MBP (red cylinders) is shown in (**a**) and (**b**), respectively, with best-fitting of the NTDs. The negatively charged side-chains of Glu153, Asp209 and Glu214 in the CTD of the minor partially-closed form of *apo* MBP (**a**) and *holo* MBP (**b**) are displayed as ball and sticks. In the *holo* MBP closed conformation potentially unfavorable interdomain electrostatic repulsion between negatively charged residues as well as lack of interdomain surface complementarity in the absence of bound sugar (cf. ref. 11, main text) precludes any significant occupancy of this closed conformation in *apo* MBP, but in the presence of bound substrate is fully compensated by the formation of numerous hydrogen bonds (both direct and water bridged) with the sugar molecule (ref. 8, main text). In the minor partially-closed form of *apo* MBP, unfavorable interdomain electrostatic repulsion is avoided by a ~6 Å translation of the CTD relative to its position in *holo* MBP, which leaves the sugar binding surface on the CTD accessible to an incoming sugar molecule.

15. Biological relevance of the minor species of *apo* MBP.

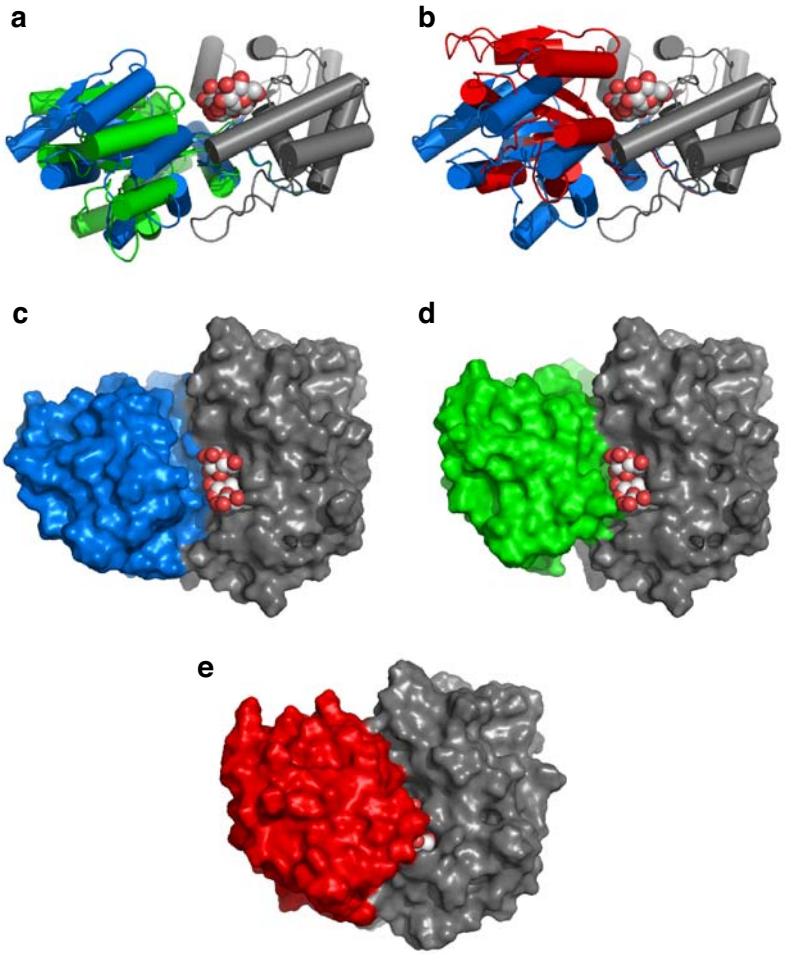

Fig. S17. Comparison of *apo* and *holo* MBP crystal structures with the minor partially-closed form of *apo* MBP derived from the PRE measurements. The CTDs are best-fitted and represented as either grey cylinders (**a** and **b**) or grey molecular surfaces (**c**, **d** and **e**). The NTD plus linker of open *apo* (1OMP), minor partially-closed *apo* and closed *holo* (3MBP) are colored in blue, red and green, respectively. (**a**) and (**b**) show the structural comparison from one perspective between open *apo* and minor *apo* and between open *apo* and closed *holo*, respectively. The structures of open *apo* (1OMP) minor partially-closed *apo* and closed *holo* (3MBP) MBP are shown from an alternative perspective (approximately 90° rotation) and in full molecular surface representation in (**c**), (**d**) and (**e**), respectively. A maltotriose molecule is depicted as ball-and-sticks and its location in the *apo* major open and minor partially-closed MBP structures is modeled by best-fitting the CTDs to the *holo* sugar-bound state. Note that the substrate is buried in *holo* MBP (**b** and **e**), but accessible in both major and minor forms of *apo* MBP (**a**, **c** and **d**) (see Table S1).

Table S1 Solvent and sugar accessible surface areas for the sugar binding surfaces of the NTD (plus linker) and CTD in major open *apo* MBP (1OMP), minor patially-closed *apo* MBP and closed *holo* MBP (3MBP).[a]

	Surface area (Å^2)					
	apo open		*apo* partially-closed		*holo* closed	
	CTD	NTD	CTD	NTD	CTD	NTD
Residues located within a 5 Å radius of maltotriose in holo MBP (3MBP)[b]						
SASA (1.6 Å probe radius)	473	226	421	69	334	58
MASA (6 Å probe radius)	314	3	265	0	90	0
Residues located within a 10 Å radius of maltotriose in holo MBP (3MBP)[c]						
SASA (1.6 Å probe radius)	1099	1214	1077	798	817	774
MASA (6 Å probe radius)	744	840	776	289	316	329

[a]SASA, solvent accessible surface area calculated with a probe radius of 1.6 Å. MASA, surface area accessible to external maltotriose calculated with a probe radius of 6 Å. The surface areas for *holo* MBP are calculated in the absence of the bound maltotriose coordinates. Surface area calculations were performed using Xplor-NIH.[S9]

[b]The residues within a 5 Å radius of the bound maltotriose substrate in *holo* MBP (3MBP) are residues 12, 14, 15, 44, 45, 62, 63, 65, 66, 111, 153, 154, 155, 156, 230, 330, 340, 341, and 344.

[c]The residues within a 10 Å radius of the bound maltotriose substrate in *holo* MBP (3MBP) are residues 11-16, 41-48, 61-67, 69-70, 109-113, 150-159, 209-210, 226-231, 257-263, 297-300, 330-333, 340-348, and 367.

16. Kinetics of ligand binding.

Bacterial periplasmic binding proteins (bPBP) have been classified into two classes on the basis of their β-sheet topologies. In the type I family, the sheet topology of both domains is of the form $\beta_2\beta_1\beta_3\beta_4\beta_5$; in the type II family, of which MBP is a member, the sheet topology is $\beta_2\beta_1\beta_3\beta_n\beta_4$ where β_n is the strand just after the first cross-over from the NTD to the CTD, and vice versa.[S1] Outside the β-sheets there is extensive structural variation among the members of each family.

In the case of MBP,[S2,S3] as well as most bPBPs,[S3-S6] the observed rate constant, k_{obs}, measured by stopped-flow experiments, is proportional to ligand concentration, and the kinetic data can therefore be accounted for by a simple one-step binding mechanism. This simply means that the transition between *apo* open and *apo* partially-closed states of MBP is extremely rapid, as is indeed the case experimentally from relaxation dispersion and $\{^{15}N\}$-^{1}H NOE data which place the exchange rate within a time range spanning from 20 ns to 20 μs (see main text and methods). In the case of C4-dicarboxylate binding protein (DctP), another member of the type II bPBP family, k_{obs} decreases in a hyperbolic manner with increasing ligand concentration, and analysis of the stopped flow data provide kinetic evidence that *apo* DctP exists as an equilibrium between a major non-binding (94-97%) form and a minor (3-6%) ligand-binding state.[S7,S8] The exchange rate between these two putative species is ~1 ms which is at least 2-3 orders of magnitude slower than that for the transition between *apo* open and *apo* partially-closed MBP. The DctP data were interpreted to imply, without any experimental evidence, that the major open form of DctP was in a closed conformation while the minor open form that actually bound ligand represented the open conformation.[S7,S8]

17. Comparison with the *apo* form of the type I bPBP glucose/galactose binding protein (GGBP).

GGBP is a member of the type I family of bPBPs, and as noted above in Section 16 the domains of the type I and type II bPBPs are topologically very different. In contrast to MBP where the *apo* state has only been crystallized in an open conformation (1OMP[S9]), the first crystal structure of apo GGBP reported was that of a closed form that was virtually identical to that of the closed ligand-bound holo conformation, with a difference in relative domain orientation of only 1.8°, and water molecules bridging hydrogen bonds between the domains in a manner analogous to the sugar substrate.[S10] These crystallographic data, demonstrate that a closed holo conformation of apo GBPP is energetically accessible but provide no indication of its actual occupancy in solution. Subsequent solution SAXS data on *apo* GBPP were found to be consistent with a multitude of open conformations indicative of conformational heterogeneity,[S11] and a recently published crystal structure of an open form of *apo* GBPP shows no apparent stabilizing

interactions between the two domains.[S12] Interestingly, several open states with minimal interdomain interactions have been observed crystallographically for the related ribose binding (RBP)[S13] and allose-binding (ALBP)[S14] proteins. These results lead one to hypothesize that in solution there is extensive, possibly even largely unrestricted, interdomain motion in unliganded GBPP, as well as perhaps in RBP and ALBP. Not surprisingly, therefore, the closed *holo* conformation can be accessed in the absence of bound ligand and the complementary nature of the residues at the interdomain interface constituting the sugar binding site can be transiently stabilized via hydrogen bonds involving bridging water molecules, fulfilling essentially the smae role as the natural ligand. Large scale interdomain motions in *apo* GBPP could be ascertained experimentally from RDC measurements which would yield different alignment tensors for the two domains under such circumstances.[S15] In contrast, to GBPP, RBP and ALBP, the *apo* open state of MBP is characterized by extensive interdomain interactions (not present in the *holo* closed state), at an interface located on the opposite side of the molecule from the ligand binding cleft,[S10] which account for the observation that the open conformation observed crystallographically (1OMP)[S10] is the major form (~95%) in solution as judged by both RDC (Fig. S1a)[S16] and SAXS (Fig. S2a) measurements, as well as the present PRE data.

Supplementary references

S1. Fukami-Kobayashi, K., Tateno, T. & Nishikawa, K. Domain discloation: a change of core structure in periplasmic binding proteins in their evolutionary history. *J. Mol. Biol.* **286**, 279-290 (1999).

S2. Quiocho, F. A., Spurlino, J. C. and Rodseth, Extensive features of tight oligosaccharide binding revealed in high-resolution structures of the maltodextrin transport/chemosensory receptor. *Structure* **5**, 997-1015 (1997).

S3. Miller, D. M., Olson, J. S., Pflugrath, J. W. & Quiocho, F. A. Rates of ligand binding to periplasmic proteins involved in bacterial transport and chemotaxis. *J. Biol. Chem.* **258**, 13665-13672 (1983).

S4. Miller, D. M., Olson, J. S. & Quiocho, F. A. The mechanism of sugar binding to the periplasmic receptor for galactose chemotaxis and transport in *Escherichia coli*. *J. Biol. Chem.* **255**, 2465-2471.

S5. Ledvina, P. S., Tsai, A. L., Wang, Z., Koehl, E. & Quiocho, F. A. Dominant role of local dipolar interactions in phosphate binding to a receptor cleft with an electronegtaive charge surface: equilibrium, kinetic, and crystallographic studies. *Protein Sci.* **7**, 2550-2559 (1998).

S6. Müller, A., Severi, E., Mulligan, C., Watts, A. G., Kely, D. J., Wilson, K. S., Wilkinson, A. J. & Thomas, G. H. Conservation of structure and mechanism in primary and secondary transporters exemplified by SiaP, a sialic acid binding virulence factor from Haemophilus influenzae. *J. Biol. Chem.* **282**, 22212-22222 (2006).

16. Kinetics of ligand binding.

Bacterial periplasmic binding proteins (bPBP) have been classified into two classes on the basis of their β-sheet topologies. In the type I family, the sheet topology of both domains is of the form $\beta_2\beta_1\beta_3\beta_4\beta_5$; in the type II family, of which MBP is a member, the sheet topology is $\beta_2\beta_1\beta_3\beta_n\beta_4$ where β_n is the strand just after the first cross-over from the NTD to the CTD, and vice versa.[S1] Outside the β-sheets there is extensive structural variation among the members of each family.

In the case of MBP,[S2,S3] as well as most bPBPs,[S3-S6] the observed rate constant, k_{obs}, measured by stopped-flow experiments, is proportional to ligand concentration, and the kinetic data can therefore be accounted for by a simple one-step binding mechanism. This simply means that the transition between *apo* open and *apo* partially-closed states of MBP is extremely rapid, as is indeed the case experimentally from relaxation dispersion and $\{^{15}N\}$-^{1}H NOE data which place the exchange rate within a time range spanning from 20 ns to 20 μs (see main text and methods). In the case of C4-dicarboxylate binding protein (DctP), another member of the type II bPBP family, k_{obs} decreases in a hyperbolic manner with increasing ligand concentration, and analysis of the stopped flow data provide kinetic evidence that *apo* DctP exists as an equilibrium between a major non-binding (94-97%) form and a minor (3-6%) ligand-binding state.[S7,S8] The exchange rate between these two putative species is ~1 ms which is at least 2-3 orders of magnitude slower than that for the transition between *apo* open and *apo* partially-closed MBP. The DctP data were interpreted to imply, without any experimental evidence, that the major open form of DctP was in a closed conformation while the minor open form that actually bound ligand represented the open conformation.[S7,S8]

17. Comparison with the *apo* form of the type I bPBP glucose/galactose binding protein (GGBP).

GGBP is a member of the type I family of bPBPs, and as noted above in Section 16 the domains of the type I and type II bPBPs are topologically very different. In contrast to MBP where the *apo* state has only been crystallized in an open conformation (1OMP[S9]), the first crystal structure of apo GGBP reported was that of a closed form that was virtually identical to that of the closed ligand-bound holo conformation, with a difference in relative domain orientation of only 1.8°, and water molecules bridging hydrogen bonds between the domains in a manner analogous to the sugar substrate.[S10] These crystallographic data, demonstrate that a closed holo conformation of apo GBPP is energetically accessible but provide no indication of its actual occupancy in solution. Subsequent solution SAXS data on *apo* GBPP were found to be consistent with a multitude of open conformations indicative of conformational heterogeneity,[S11] and a recently published crystal structure of an open form of *apo* GBPP shows no apparent stabilizing